Regular aricles

Damage and fracture in thin metal sheets: New biaxial experiments

Steffen Gerke [a],[*], Fabuer R. Valencia [a], Roman Norz [b], Wolfram Volk [b], Michael Brünig [a]

[a] Institute of Mechanics and Structural Analysis, University of the Bundeswehr Munich, Werner-Heisenberg-Weg 39, D-85577 Neubiberg, Germany
[b] Chair of Metal Forming and Casting, Technical University of Munich (TUM), Walther-Meissner-Str. 4, D-85748 Garching, Germany

ARTICLE INFO

ABSTRACT

In the paper new biaxial specimen geometries for thin ductile sheet metals are proposed. The design focuses on the stress-dependent damage and failure behavior. A plastic anisotropic material model based on Hill's yield criterion and corresponding associated flow rule is presented and the related material parameters are given. Accompanying numerical simulations reveal the stress state and relate the damage mechanisms to the loading condition. The different proposed specimen geometries indicate various effects on the localization of inelastic strains, the material orientation as well as on the damage and fracture processes. During the biaxial tests strain fields in regions of interest are monitored by digital image correlation and after the experiments pictures of the fracture surfaces are taken by scanning electron microscopy and related to the stress dependent damage and failure precesses. The experimental and numerical results demonstrate the high potential of the newly developed biaxially loaded specimens.

1. Introduction

Modern industrial products have to fulfill demands concerning improvement of cost efficiency, reduction in energy consumption as well as increase in lifetime and safety. Therefore, in lightweight applications high quality metals and alloys have been developed. For example, different aluminum alloys are employed in aeronautical and automotive industry due to their lightness and quality. However, in these thin structures often different stress-state-dependent failure processes appear during loading often causing end of life. Therefore, optimization of material properties and forming operations is required to avoid undesired damage and fracture events on micro- and macro-scales and to reduce localization of inelastic deformations under expected loading conditions.

Detailed analysis of irreversible deformations as well as of damage and fracture behavior of these metals and alloys is required to understand and to optimize manufacturing processes. In this context, accurate and practically applicable constitutive models and corresponding efficient numerical approaches have to be developed to create new or to improve existing engineering production processes. To detect stress-state- and loading-direction-dependent material behavior experiments taking into account different loading directions with respect to the principal axes of anisotropy as well as a wide range of multi-axial loading conditions have to be performed. Focus of the new experimental–numerical analysis discussed in the present paper is on development of new biaxially loaded specimens cut from thin

anisotropic metal sheets to reveal damage and failure mechanisms depending on stress state and loading direction.

Caused by multi-stage manufacturing processes during production of thin metal sheets anisotropies occur as a result of internal changes in the crystallographic structures. It is worthy to note that scatter of experimental data occur caused by testing techniques, limitations in precision of manufacturing of specimens, deviations in machine precision or statistical variation in material properties. Therefore, phenomenological material approaches shall predict the essential experimentally observed features. In this context, generalized macroscopic plasticity models have been developed to take into account the deformation-induced anisotropies. For example, yield criteria with quadratic functions of stresses have been developed by Hill (1948) and Stoughton and Yoon (2009). Since in some cases these constitutive approaches lead to unsatisfactory results yield conditions with higher-order stress functions have been presented by Barlat et al. (2005), Ha et al. (2018), Tsutamori et al. (2020) and Hu et al. (2021) to simulate anisotropic plastic behavior of ductile metals.

Different experiments with uniaxially and biaxially loaded specimens have been discussed in the literature to study formation of inelastic deformations as well as damage and fracture behavior on the micro- and macro-scales. For example, to analyze in detail the effect of stress state on damage and fracture processes experiments with unnotched and differently notched uniaxially loaded specimens have

been performed by Bai and Wierzbicki (2008), Brünig et al. (2008), Driemeier et al. (2010), Gao et al. (2010), Li et al. (2011) and Dunand and Mohr (2011). Currently, test specimens with heterogeneous stress and strain fields for inverse determination of material parameters are receiving increasing attention, see e.g. Pierron and Grédiac (2021) and Cauvin et al. (2022), where promising new approaches can be expected in the future. In addition, special geometries of flat specimens have been discussed by Brünig et al. (2008), Roth and Mohr (2016), Lou et al. (2017) and Liu et al. (2019) to examine shear-dominated stress states. However, these tests with uniaxially loaded specimens only cover a small range of relevant stress states and, therefore, extended experimental programs with biaxially tested cruciform specimens have been proposed by Lin and Ding (1995), Green et al. (2004), Kuwabara (2007) and Kulawinski et al. (2011). In addition, newly designed biaxially loaded flat specimens have been developed by Gerke et al. (2017) and Brünig et al. (2015, 2019, 2020). Recently, these biaxial experiments have been applied by Brünig et al. (2021, 2022) to study the behavior of anisotropic metals. These biaxially loaded specimens are taken from thin sheets with 3–5 mm thickness and to localize inelastic deformations notches in thickness direction have been added in desired regions. However, this reduction in thickness cannot be applied in thin sheets of about 1 mm thickness or less. As a consequence, new geometry details have to be developed to be able to cause localization of inelastic deformations as well as occurrence of damage and failure in regions of interest.

In the present paper the elastic–plastic constitutive model for anisotropic metals is presented and identification of material parameters for the investigated aluminum alloy AA6016-T4 is discussed. New specimen designs cut from 1 mm thick sheets are discussed to analyze stress-state-dependent damage and failure mechanisms in regions of interest. Experimental results are compared with those from corresponding numerical simulations demonstrating the efficiency of the new specimens.

2. Material model

The proposed phenomenological material model is based on experimental observations on the macro-scale (Brünig et al., 2021, 2022). Modeling of elastic–plastic deformation behavior takes into account the additive decomposition of the strain rate tensor $\dot{\mathbf{H}}$ into an elastic $\dot{\mathbf{H}}^{\mathrm{el}}$ and a plastic part $\dot{\mathbf{H}}^{\mathrm{pl}}$. Elastic behavior is assumed to be isotropic and governed by Hooke's law whereas the anisotropic plastic behavior for thin metal sheets is characterized by the Hill yield condition

$$f^{\mathrm{pl}} = \left\{ \frac{1}{2}\left[(G+H)\bar{T}_x^2 - 2H\bar{T}_x\bar{T}_y + (F+H)\bar{T}_y^2\right] + N\bar{T}_{xy}^2 \right\}^{1/2} - \bar{c} = 0 \tag{1}$$

assuming plane stress conditions. In Eq. (1), $\bar{T}_i$ represent the respective components of the Kirchhoff stress tensor, F, G, H and N are the anisotropy parameters identified by different uniaxial experiments and $\bar{c}$ denotes the equivalent stress measure which in the present approach is taken to be the tensile yield stress of the uniaxial specimen cut in rolling direction, $\bar{c} = \bar{c}_x$. In the analysis the evolution of this equivalent stress measure is modeled by the Voce law

$$\bar{c} = c_o + R_o \epsilon^{\mathrm{pl}} + R_\infty \left(1 - e^{-b\,\epsilon^{\mathrm{pl}}}\right) \tag{2}$$

where c_o represents the initial yield stress, R_o and R_∞ are hardening moduli, b denotes the hardening exponent and ϵ^{pl} means the equivalent plastic strain measure. In addition, performing tension tests with specimens cut in transverse direction the yield stress $\bar{c}_y$ is identified and shear tests with uniaxially loaded specimens cut in rolling direction

lead to the yield stress $\bar{c}_{xy}$. Then, the anisotropy parameters

$$F = \frac{2\bar{c}}{\bar{c}_y} \quad \text{and}$$

$$N = \left(\frac{\bar{c}}{\bar{c}_{xy}}\right)^2 \tag{3}$$

are directly given from Eq. (1).

Furthermore, plastic strains occurring during the loading process are determined by the associated flow rule

$$\dot{\mathbf{H}}^{\mathrm{pl}} = \dot{\lambda}\frac{\partial f^{\mathrm{pl}}}{\partial \bar{\mathbf{T}}} \tag{4}$$

leading to the respective components

$$\dot{H}_x^{\mathrm{pl}} = \dot{\lambda}\left[(G+H)\bar{T}_x - H\bar{T}_y\right]$$
$$\dot{H}_y^{\mathrm{pl}} = \dot{\lambda}\left[(F+H)\bar{T}_y - H\bar{T}_x\right] \tag{5}$$
$$\dot{H}_{xy}^{\mathrm{pl}} = \dot{\lambda}N\bar{T}_{xy}$$

where $\dot{\lambda}$ is the scalar-valued plastic equivalent strain rate measure describing the amount of plastic strains. Assuming isochoric plastic deformation behavior the plastic strain rate in thickness direction is given by

$$\dot{H}_z^{\mathrm{pl}} = -\left(\dot{H}_x^{\mathrm{pl}} + \dot{H}_y^{\mathrm{pl}}\right) = \dot{\lambda}\left(G\bar{T}_x + F\bar{T}_y\right). \tag{6}$$

To determine the material parameters of the proposed elastic–plastic model, different uniaxial tensile tests are performed with specimens cut at an angle φ to the rolling direction of the sheet. The yield stresses in the main directions of material anisotropy can then be expressed, for example, in the following form

$$\bar{T}_x = \bar{T}_\varphi \cos^2\varphi, \quad \bar{T}_y = \bar{T}_\varphi \sin^2\varphi \quad \text{and}$$
$$\bar{T}_{xy} = \bar{T}_\varphi \sin\varphi\cos\varphi, \tag{7}$$

where $\bar{T}_\varphi$ is the tensile yield stress in the φ-direction. With Eqs. (5) and (6) the corresponding plastic strain rates are

$$\dot{H}_x^{\mathrm{pl}} = \dot{\lambda}\left[(G+H)\cos^2\varphi - H\sin^2\varphi\right]\bar{T}_\varphi$$
$$\dot{H}_y^{\mathrm{pl}} = \dot{\lambda}\left[(F+H)\sin^2\varphi - H\cos^2\varphi\right]\bar{T}_\varphi$$
$$\dot{H}_{xy}^{\mathrm{pl}} = \dot{\lambda}N\sin\varphi\cos\varphi\,\bar{T}_\varphi \tag{8}$$
$$\dot{H}_z^{\mathrm{pl}} = -\dot{\lambda}\left(G\cos^2\varphi + F\sin^2\varphi\right)\bar{T}_\varphi$$

An alternative indirect approach to the determination of the anisotropy parameters is based on the evaluation of the ratios of the measured plastic strain increments in tensile specimens cut in the x- direction (RD, 0°) and y-direction (TD, 90°) of the sheet metal as well as in its diagonal direction (DD, 45°). Using the transformation of the plastic strain rates to the specimen's orientation φ and the corresponding transverse direction ($\varphi + 90°$) the respective strain rates are given by

$$\dot{H}_\varphi^{\mathrm{pl}} = \dot{H}_x^{\mathrm{pl}}\cos^2\varphi + \dot{H}_y^{\mathrm{pl}}\sin^2\varphi + 2\dot{H}_{xy}^{\mathrm{pl}}\sin\varphi\cos\varphi$$
$$\dot{H}_{\varphi+90°}^{\mathrm{pl}} = \dot{H}_x^{\mathrm{pl}}\sin^2\varphi + \dot{H}_y^{\mathrm{pl}}\cos^2\varphi - 2\dot{H}_{xy}^{\mathrm{pl}}\sin\varphi\cos\varphi \tag{9}$$

and with Eq. (8) the requested plastic strain rate can be expressed in the form

$$\dot{H}_{\varphi+90°}^{\mathrm{pl}} = \dot{\lambda}\bar{T}_\varphi\left[-H + (G+F-2N+4H)\sin^\varphi\cos^2\varphi\right]. \tag{10}$$

In thin metal sheets determination of material parameters related to the anisotropy of the material is usually restricted to tests with specimens cut in its plane. Recalling that different experiments with uniaxial tension specimens cut at an angle φ with respect to the rolling direction are taken into account. This leads to the definition of the Lankford coefficients (r-values)

$$r_\varphi = \frac{\dot{H}_{\varphi+90°}^{\mathrm{pl}}}{\dot{H}_z^{\mathrm{pl}}} = \frac{-\dot{H}_{\varphi+90°}^{\mathrm{pl}}}{\dot{H}_x^{\mathrm{pl}} + \dot{H}_y^{\mathrm{pl}}} \tag{11}$$
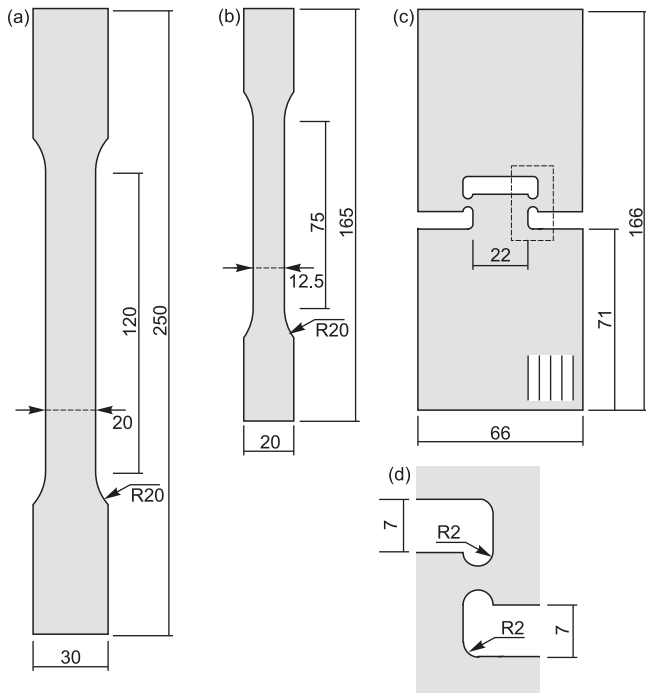
Fig. 1. One-dimensionally loaded specimens: (a) flat bar tension specimen 1, (b) flat bar tension specimen 2, (c) shear specimen and (d) detail of the shear specimen; all measures in [mm].

Table 1
Chemical decomposition based on a cast analysis aluminum alloy AA6016-T4, 1 mm.

Si	Fe	Cu	Mn
1.200	0.238	0.079	0.138
Mg	Cr	Zn	Ti
0.384	0.019	0.014	0.020

which, alternatively, can be written with Eqs. (8) and (10) in the form

$$r_\varphi = \frac{H + (2N - F - G - 4H)\sin^2\varphi\cos^2\varphi}{F\sin^2\varphi + G\cos^2\varphi}, \qquad (12)$$

see Brünig et al. (2021, 2022) for further details.

Evaluating the yield condition (Eq. (1)) for tensile loading in x-direction ($\bar{T}_x = \bar{c}_x$ and $\bar{T}_y = \bar{T}_{xy} = 0$) for the anisotropy coefficients G and H

$$H = 2 - G \qquad (13)$$

is directly derived. Furthermore, considering the r-values (Eq. (12)) with respect to the rolling (RD, 0°), the transverse (TD, 90°) and the diagonal direction (DD, 45°) this leads to the additional relations between the anisotropy coefficients

$$G = \frac{2}{\left(1 + r_{0°}\right)}$$
$$F = \frac{H}{r_{90°}} \quad \text{and} \qquad (14)$$
$$N = \left(\frac{1}{2} + r_{45°}\right)(F + G).$$

It should be noted that the parameters F and N can alternatively be determined by considering the yield stresses of uniaxial tension and shear tests, see Eq. (3). Brünig et al. (2022) suggested to use the mean value of Eqs. (3) and (14) showing good numerical results compared with experimental data for an aluminum alloy of series 2000.

The investigated ductile metal is the aluminum alloy AA6016-T4 with the chemical composition listed in Table 1. Experiments with
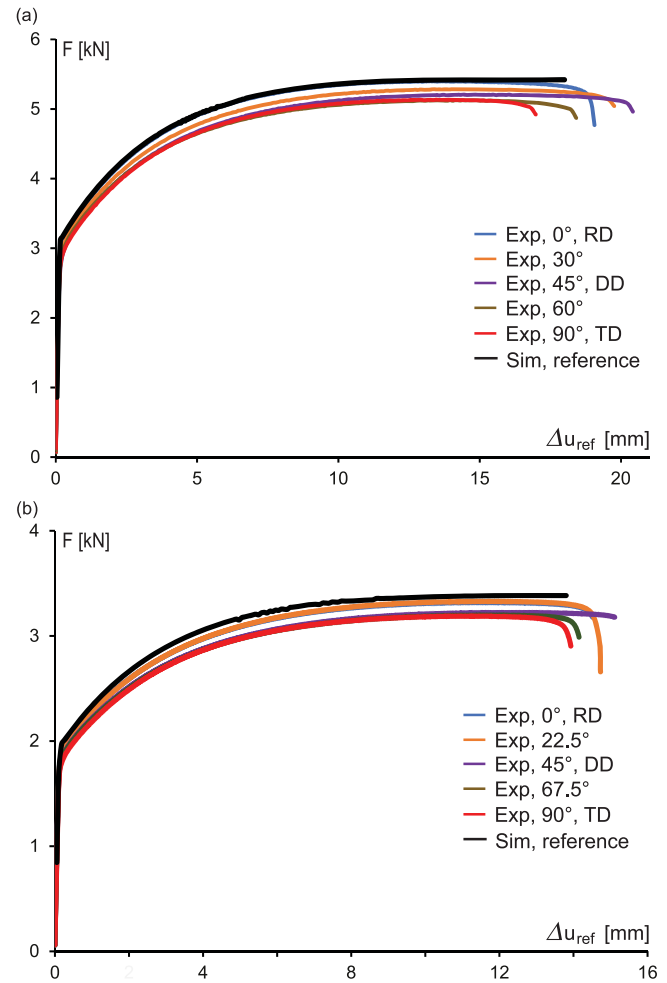

Fig. 2. Load–displacement-curves: (a) extracted from experiments with flat bar tension specimen 1 (see Fig. 1(a)) and (b) from experiments with flat bar tension specimen 2 (see Fig. 1(b)).
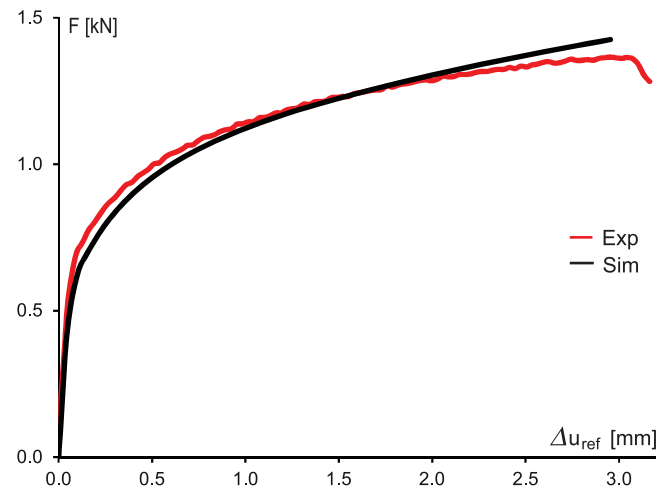

Fig. 3. Load–displacement-curves extracted from shear experiments with shear specimen 1 (see Fig. 1(c)).

uniaxially loaded specimens cut in different directions with respect to the loading direction from 1 mm thick sheets are performed to identify material parameters. Measurement of three-dimensional displacement
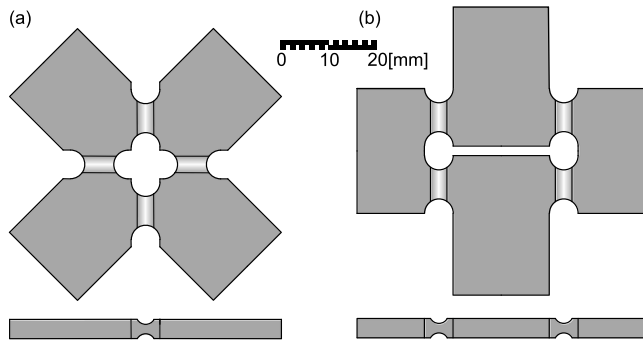
Fig. 4. (a) X0-specimen (b) H-specimen.

Table 2
Material parameters of the aluminum alloy AA6016-T4, 1 mm.

K [MPa]	E [MPa]	c_0 [MPa]	R_0 [MPa]	R_∞ [MPa]	b [−]
57 500	69 000	155	260	130	16

Table 3
Lankford coefficients for the aluminum alloy AA6016-T4, 1 mm.

$r_{0°}$	$r_{45°}$	$r_{90°}$
0.6827	0.4369	0.6333

Fig. 5. New biaxial specimens: (a) drawing 22.5°; photos (b) 0°, (c) 22.5° and (d) 45°; all measures in [mm].

fields on respective surfaces of the specimens are monitored by digital image correlation. This leads to plastic strain increments which can be used to determine the *r*-values during the loading process. In particular, two tensile specimens with initial length of 250 mm and 165 mm as well as the symmetric shear specimen shown in Fig. 1 are tested. During loading of the specimens the load–displacement curves shown in Figs. 2 and 3 are recorded. The experiments with the specimens shown in Fig. 1(b) were carried out at TUM and the experiments with the specimens shown in Fig. 1(a) were carried out at the University of the Bundeswehr Munich. Associated load–displacement curves are shown in Fig. 2(a) and (b) and indicate the same trends regarding loading direction and consequently reflect the independence of the results from the specimen size. For the aluminum alloy under investigation highest load is measured for loading in rolling direction (0°) and with increasing angle a decrease in maximum load of about 6% can be seen.

From the uniaxial tension test with the specimen cut in rolling direction the bulk modulus *K* and Young's modulus *E* characterizing the elastic behavior as well as the parameters in Eq. (2) describing uniaxial plastic yielding are determined, see Table 2. This allows numerical simulation of the load–displacement curves of the reference tensile tests with the specimen cut in rolling direction showing good agreement with the experimental results.

Based on the digital image correlation measurement during the tensile test with the specimen cut in rolling direction the plastic strain rates can be determined. Taking into account Eq. (11) they are used to identify the Lankford coefficients listed in Table 3. These coefficients clearly demonstrate the anisotropy of the investigated thin aluminum alloy sheet.

Using the Lankford coefficients and the yield stresses obtained from the tensile and shear tests the anisotropy parameters of the aluminum alloy AA6016-T4 can be computed (see Table 4). This allows numerical simulation of different experiments with uniaxially and biaxially loaded specimens cut from thin sheets. For example, numerical simulation of the shear test shows good agreement with the experimental curve shown in Fig. 3. Further results of numerical analysis of newly developed biaxially loaded specimens will be discussed in the next sections.
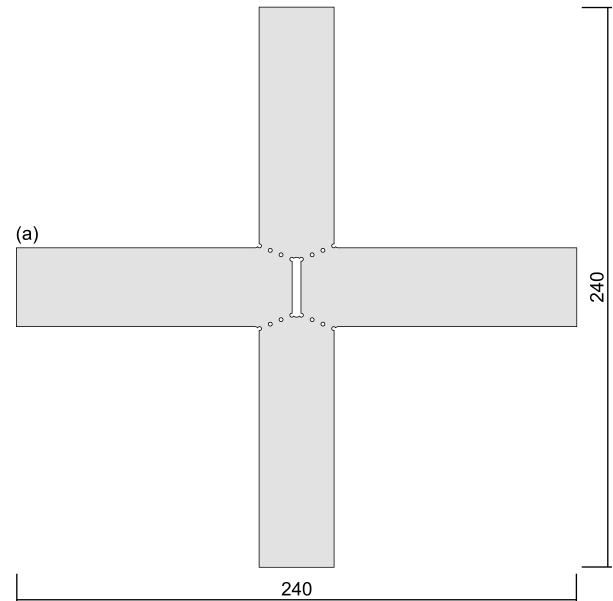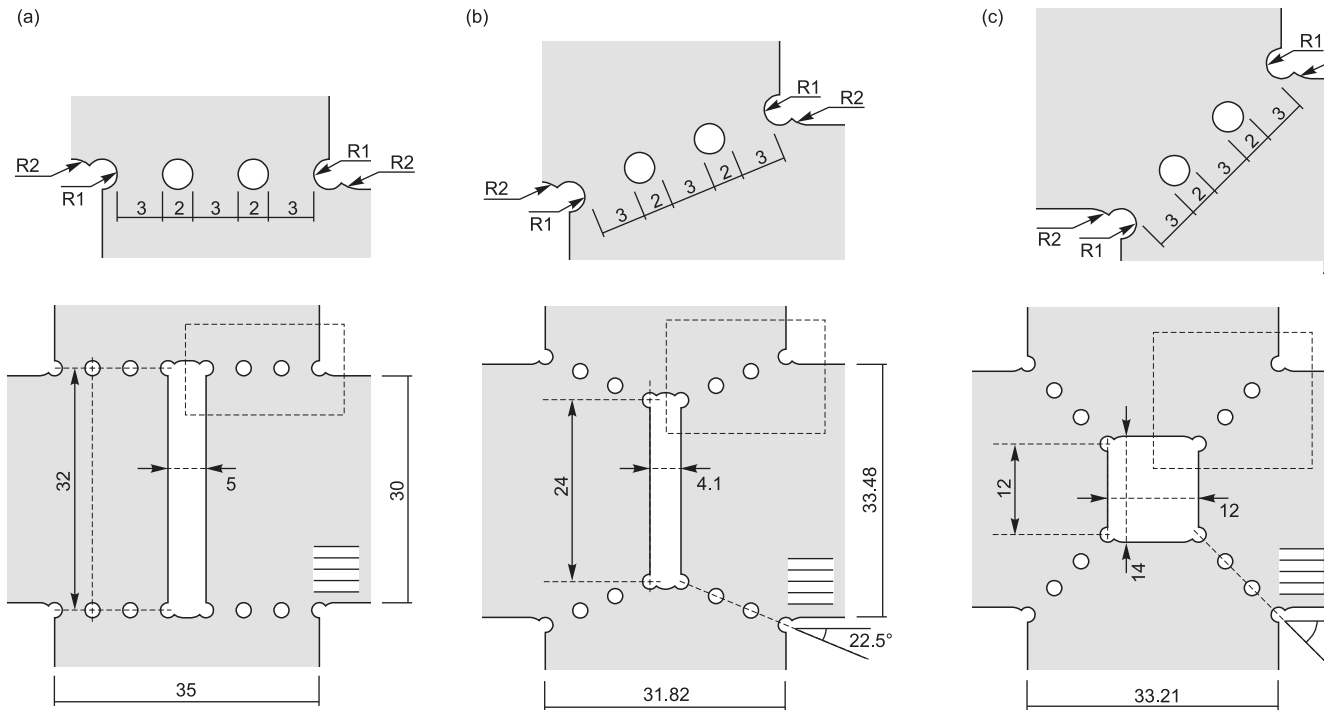
Fig. 6. Details of biaxial geometries: (a) 0°, (b) 22.5° and (c) 45°; all measures in [mm].

Fig. 7. Biaxial testing machine and DIC system.

Fig. 8. Notation of biaxial experiments. (For interpretation of the references to color in this figure legend, the reader is referred to the web version of this article.)

Table 4
Anisotropy parameters of the aluminum alloy AA6016-T4, 1 mm.

F [−]	G [−]	H [−]	L [−]	M [−]	N [−]
1.3619	1.1885	0.8114	3	3	2.3267

Combined with the validation of the related material models,

3. Specimen design

For the systematic investigation of the stress-state-dependent damage and fracture behavior of ductile sheet metal, carefully designed and selected specimens have to be applied. In this context, biaxial geometries have the advantage that different stress states can be generated
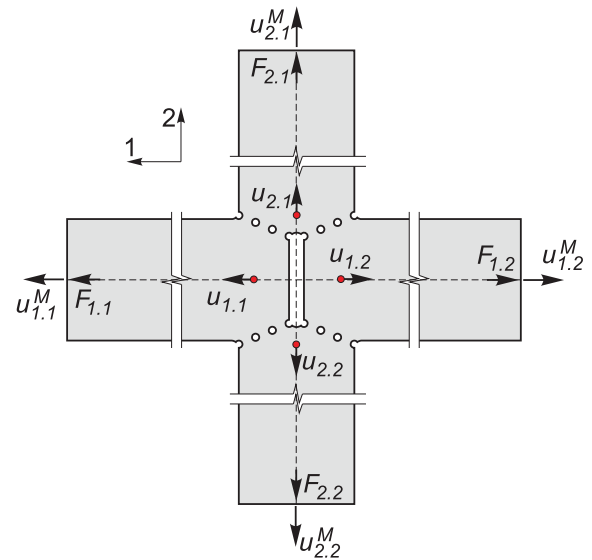
based on the applied loads and that material orientation can be taken into account, see for instance (Mamros et al., 2022; Daehn et al., 2021; Brünig et al., 2022). In the design of the new biaxial specimens the following aspects can be understood as a guiding principle, see for a detailed discussion for example (Gerke et al., 2017, 2020):

- That with one specimen geometry the material behavior under different loading conditions can be investigated in a controlled manner. This enables non-proportional loading paths and reduces the manufacturing costs.
- Symmetrical test specimens facilitate a symmetrical test execution especially under simultaneous loading of both axes. The
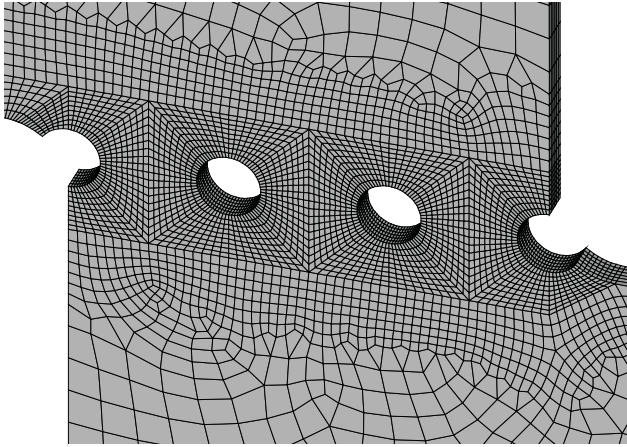
Fig. 9. Finite element mesh: three-dimensional perspective on perforated part of the 0° specimen.

sheet center plane and the planes that are spanned by the machine axes perpendicular to the sheet plane are essential here. If the axles are loaded exclusively independently of each other, biaxially extended shear test specimens are possible, see e.g. Driemeier et al. (2010), Wang et al. (2022) and Kong et al. (2022), but only one axis should be clamped at a time to protect the machine in the event of unplanned failure or uncontrolled machine displacement.

- In case of unscheduled movement of the biaxial machine, the test body must fail before it results in damage to the machine. Stiff couplings of the machine connectors must be avoided.
- The region of interest (ROI) should be as compact as possible to reasonably use the resolution of the digital image correlation (DIC) system.
- It is advantageous that the biaxial loading of the specimen has a comprehensible relation to the stress state in the region of interest of the specimen. This allows during practical testing a direct estimation of the progress of the experiment which becomes more beneficial under load path changes.
- The production of the test specimens should be as simple as possible. On the one hand, this keeps manufacturing costs low and, on the other, makes reproducibility in production simpler.

The X0-specimen and the H-specimen (Fig. 4) have been successfully used to investigate the damage and failure behavior of sheets with a thickness of 4 mm (Gerke et al., 2019; Brünig et al., 2019). Both geometries have a similar topology characterized by a central opening and four notched regions where damage and failure occur. The main difference between the geometries is the orientation of the notches whereby other orientations are also possible. This notch orientation allows in conjunction with the applied load control the stress state in the notched regions. In the case of the thin sheets of aluminum with a thickness of 1 mm considered here, it is no longer possible to insert a notch in thickness direction to determine the strain localization. In addition, significant changes in the grain structure over the thickness can occur due to the manufacturing process of the sheet metal, so that the insertion of notches does not appear to appropriate taking into account this aspect. Thus, significant changes of the specimen topology have to be realized, i.e. the X0- and H-specimens cannot be adapted. Consequently, new possibilities must be found for the design of specimens geometries for thin sheet metal in order to predetermine the strain localization in a certain area without notches in thickness direction. In addition, it has to be considered that testing under different loading conditions and loading directions with respect to the main axes of

material anisotropy is possible with the newly presented specimens geometries.

Material anisotropy plays a decisive role in the design of new biaxial test specimens for thin sheets. In Brünig et al. (2022) the possibility is presented to manufacture geometrically equal test specimens in different directions to the main axes of material anisotropy and to test them under equal proportional loading conditions. Starting from the base material, which is available in quadratic cutouts with dimensions of 240 by 240 mm, this procedure has proven to be costly from the manufacturing side, so that the production of different geometries with differently orientated localization areas seems to be more reasonable. As described above, the X0- and H-specimens presented for sheets with 4 mm can be interpreted in this way by taking intermediate steps of notch inclination into account.

For notched tensile specimens, the radius at the taper point determines the region of increased distortion (Bai and Wierzbicki, 2008; Brünig et al., 2008; Gao et al., 2005). A larger radius leads to a more extended region of increased strain, and a smaller radius leads to a more concentrated region (Driemeier et al., 2010). A similar effect can be observed in tensile test specimens with a central hole (Roth and Mohr, 2016). Thus, the insertion of holes in combination with lateral notches represents a suitable possibility to predefine the area with increased inelastic strains. Based on these considerations, for the aluminum sheet with a thickness of 1 mm investigated here, the specimen design shown in Fig. 5 has been chosen. The external dimensions are again taken to be 240 by 240 mm for all geometries, and the radius of the holes and notches introduced is 1.0 mm. The three geometries (Fig. 5(b–d)) are characterized by a central opening, which gives four weakened areas for each geometry. Each area consists of three connectors separated by holes. The arrangement of the drillings differs here in the angle to the horizontally displayed axis with 0°, 22.5° and 45°. The geometry with 0° allocation can be understood in reference to the H-specimen and the geometry with 45° allocation in reference to the X0-specimen. The geometry with 22.5° inclination represents an intermediate step. Details of the respective geometries can be found in Fig. 6 and allow an exact reproduction of the specimens. Each of the three remaining connectors has a cross-sectional area of 3.0 mm^2, and a cross-sectional area of 9.0 mm^2 remains per connector area, making the specimens sufficiently robust to handle.

4. Experimental program

The used biaxial testing machine LFM-BIAX from Walter+Bai, Löhningen, Switzerland (Fig. 7) is equipped with four individually controllable electro-mechanical cylinders with maximum loads of 20 kN (tension and compression), where the newly designed biaxial test specimens (see Fig. 5) are clamped by means of jaws. The four force signals ($F_{i,j}$, see Fig. 8) and machine displacements ($u_{i,j}^M$, see Fig. 8) are transmitted to the digital image correlation (DIC) system provided by Limess, Krefeld, Germany (Dantec), where the machine data is stored together with that from the DIC system. The DIC system consists of four Manta G-609B/C 6 MPx cameras with Sony 6 MPx CCD sensor (2752 by 2206 px), calibrated by using the corresponding calibration target, see Fig. 7. Adequate diffuse cold light is generated by LED panels of the type Fomex FL-B50 and B25. The associated evaluation of the data is performed in the Istra4D software provided by Dantec using the 'plane' option. For the results shown below, a resolution of about 65 px/mm was achieved. The selected subset size was 33 px (square) and the overlap was 11 px, resulting in about nine evaluation points per mm^2.

In Fig. 8 the notation used here is illustrated. After the tests, nominal displacements at the points marked in red in the central area of the specimen $u_{i,j}$ are evaluated by the DIC system. The relationship between machine displacement and nominal displacements is nonlinear and dependent on the load case, since, among other things, influences from machine stiffness and slight slipping of the clamping jaws
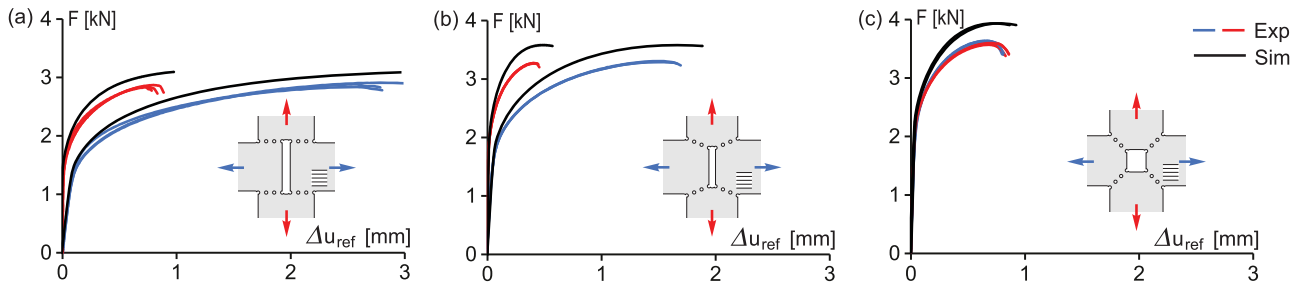
Fig. 10. Load displacement curves: (a) 0°, (b) 22.5° and (c) 45°. (For interpretation of the references to color in this figure legend, the reader is referred to the web version of this article.)
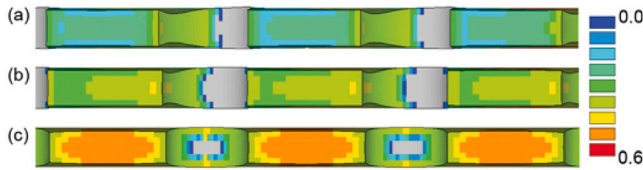

Fig. 11. Stress triaxiality η: (a) 0° at $\Delta u_{\text{ref},1} = 2.0$ mm, (b) 22.5° at $\Delta u_{\text{ref},1} = 1.3$ mm and (c) 45° at $\Delta u_{\text{ref},1} = 0.7$ mm.
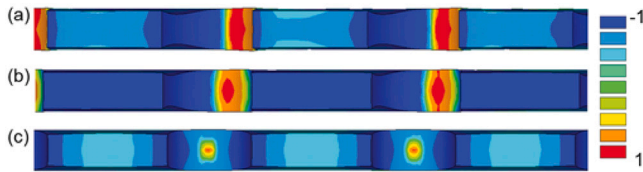
Fig. 12. Lode parameter ω: (a) 0° at $\Delta u_{\text{ref},1} = 2.0$ mm, (b) 22.5° at $\Delta u_{\text{ref},1} = 1.3$ mm and (c) 45° at $\Delta u_{\text{ref},1} = 0.7$ mm.
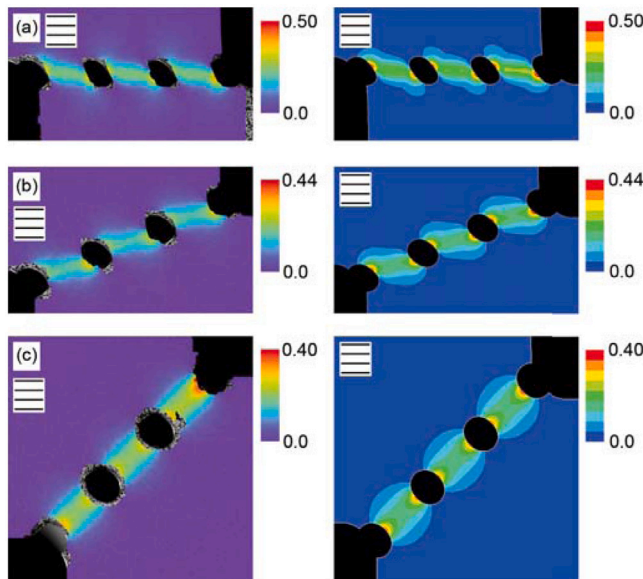

Fig. 13. First principal strain, left side: experimental data (DIC), right side numerically calculated: (a) 0° at $\Delta u_{\text{ref},1} = 2.0$ mm, (b) 22.5° at $\Delta u_{\text{ref},1} = 1.3$ mm and (c) 45° at $\Delta u_{\text{ref},1} = 0.7$ mm.

enter and vary slightly between the experiments of each geometry. Furthermore, the averaged forces per axis are introduced

$$F_i = \frac{F_{i.1} + F_{i.2}}{2} \tag{15}$$

as well as the relative displacements on the axes

$$\Delta u_{\text{ref}.i} = u_{i.1} + u_{i.2} \tag{16}$$

as adequate displacement measure for data interpretation (Fig. 8).

In addition to symmetrical test specimens, a test routine that also remains almost symmetrical during the test sequence is essential. The main idea of the test routine used here is to maintain a constant load ratio. For this purpose, axis 1 is used leading and axis 2 following almost simultaneously (Gerke et al., 2017, 2019). In summary, this can be described as follows:

- Cylinder 1.1 is controlled at constant speed of 0.04 mm/s. This causes the machine displacements $u_{1.1}^{\text{M}}$.
- The opposite cylinder 1.2 receives the same machine displacement $u_{1.2}^{\text{M}} = u_{1.1}^{\text{M}}$.
- Cylinder 2.1 is controlled by the force $F_{2.1} = \zeta F_1$, where ζ is a constant load factor. This results in the machine displacement $u_{2.1}^{\text{M}}$.
- The opposite cylinder 2.2 undergoes the machine displacement $u_{2.2}^{\text{M}} = u_{2.1}^{\text{M}}$.

Thus, three of the four cylinders proceed in a displacement-controlled manner and the symmetry of the experiment is determined by the symmetrical machine displacements. The practical implementation is carried out with the control software Dion7 provided by Walter+Bai. Furthermore, for the later presentation of results the marked area shown in Fig. 6 is selected.

Corresponding numerical analysis of the respective biaxial experiments have been carried out to detect the stress states during the loading processes. For these numerical simulations the finite element program ANSYS in connection with the material model presented in Section 2 has been applied. In detail, a quarter of the specimens is divided into eight-node-elements of type SOLID185 using symmetry boundary conditions to reduce numerical costs. This results into 24 084 for the 0° (see Fig. 9), 24 042 for the 22.5° and 25 134 elements for the 45° specimen. The respective displacements are applied to the nodes at the end faces and iterated to meet the corresponding load ratio. Out-of-plane movements are neglected by zero displacements in this direction of the nodes in the symmetry planes at the end surfaces. Refinement of the finite element mesh has been realized in the perforated parts to accurately predict the expected stress states and its gradients as well as the localization of strains.

In the following, experimental and numerical results with the three geometries shown in Fig. 5 under proportional load $F_1/F_2 = 1/1$ are presented and discussed. For each geometry, the horizontally shown axis corresponds to the rolling direction of the material, which is indicated by parallel lines in the corresponding figures as well.

5. Results

The global deformation behavior of the different specimen geometries is illustrated by the load–displacement diagrams shown in Fig. 10,
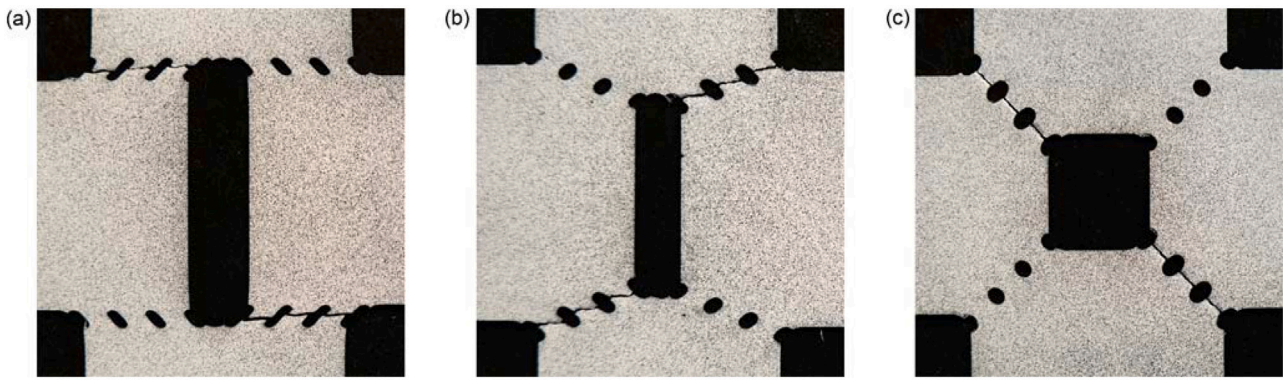
Fig. 14. Central part of fractures specimens: (a) 0°, (b) 22.5° and (c) 45°.

where F_i are the loads given by Eq. (15) and u_i are the relative displacements given by Eq. (16) of opposite measuring points of both axes lying on the symmetry axis, whereby the exact position influences the results only marginally. Shown for each specimen are the curves of 3 experiments and a corresponding simulation. The experiments show very good reproducibility and differences become obvious only shortly before failure, see in particular Fig. 10(a). The numerical calculations can reproduce the elastic–plastic behavior of the experiments qualitatively well, but for the load case $F_1/F_2 = 1/1$ considered here, they are slightly above the experimental curves. This observation in load may be a consequence of damage in the experiments which is not taken into account in the numerical analysis. The influence of the material direction becomes clear in the results illustrated here for the geometry with 45° hole alignment, see Fig. 10(c). The maximum forces in axis 2 (Fig. 10(c), red) are reached at larger relative displacements than in axis 1 (blue) and in addition the displacements at fracture are higher in axis 2.

The stress state in this context is often described by the stress triaxiality

$$\eta = \frac{\bar{\sigma}_m}{\bar{\sigma}_{eq}} = \frac{\bar{I}_1}{3\sqrt{3\bar{J}_2}} \tag{17}$$

and the Lode paramenter

$$\omega = \frac{2\bar{T}_2 - \bar{T}_1 - \bar{T}_3}{\bar{T}_1 - \bar{T}_2} \quad \text{with} \quad \bar{T}_1 \geq \bar{T}_2 \geq \bar{T}_3. \tag{18}$$

Here, $\bar{\sigma}_m$ stands for the mean stress, $\bar{\sigma}_{eq}$ for the equivalent von Mises stress and $\bar{I}_1$ for the first stress invariant, $\bar{J}_2$ for the second deviatoric invariant of the stress tensor as well as $\bar{T}_i$ represent the principal stresses.

Fig. 11 indicates the stress triaxiality and Fig. 12 the Lode parameter in the area of the holes on the cross-section at approximately 70% of the maximum displacement. Here, the three connectors of an area show very similar distributions for each particular geometry, which are also very homogeneous distributed. For the geometry with 0° arrangement of the holes, the numerical simulation shows stress triaxialities in the range of 0.15 to 0.22 (Fig. 11(a)) which indicates that this is in the range of a shear stress state superimposed by tension. As the inclination of the holes increases, the stress triaxiality increases. Thus, for the geometry with 22.5° inclination, values up to 0.36 (Fig. 11(b)) and for the geometry with 45° alignment values up to 0.52 (corresponding to a biaxial tension stress state, Fig. 11(c)) are achieved. As the inclination of the notches increases, the distribution in the stress triaxiality and the Lode parameter becomes slightly more non-uniform, see Figs. 11(c) and 12(c). The Lode parameter (Fig. 12) is in the negative range for all three geometries with values between −0.45 and −1.

A comparison of the strains measured experimentally by DIC (left column) and those determined by simulation (right column) is shown in Fig. 13. The strains were evaluated at the same point where the stress state was plotted, cf. Figs. 11 and 12. Overall, the numerical results reproduce the experimentally determined ones very well both qualitatively in type of distribution and quantitatively in maximum values. For all three geometries, the respective maximum values are located at the holes edges, with slightly higher values at the notches towards the center of the specimen and towards the outer edge. For all geometries, however, a very similar deformation behavior of the three connections for each geometry can be observed. In this context, it is crucial to note that the distortions outside the region of interest quickly decrease and here the deformations remain reversible under load. Furthermore, the four areas of interest of each specimen geometry deform approximately equally until shortly before fracture.

The final failure of the specimens occurs by rupture of mostly two diagonally located areas of interest, whereas no information can be obtained which of the connectors fails first. Fig. 14 shows the deformed and cracked specimens under 1/1 loading. These can be seen in continuation with the deformation illustrated in Fig. 13. For the specimen geometry with 45° alignment of the holes, they expand almost spherically and the crack occurs with the necking typical of tensile loading (cf. also Fig. 14(c)) and with rather uneven fracture surface. As the angle of the holes decreases and thus the shear superposition increases, the holes first become elliptical before failure (22.5°) (Fig. 14(b)) and then elongated (0°) (Fig. 14(c)). For each geometry, the crack path is oriented at the locations of the largest strains from the holes toward the middle of the connectors, see Fig. 13.

Fig. 15 shows images of the fracture surfaces taken by scanning electron microscopy (SEM) for each geometry in the center of the middle connector. The pre-fracture stress state (Figs. 11 and 12) can be well related to the damage mechanism that resulted in the crack (Brünig et al., 2013). For the geometry 0° aligned holes sheared dimples indicate shear stresses superimposed by tension (Fig. 15(a)) whereas for the geometry 22.5° a rather ductile damage behavior is indicated with significant void growth before fracture, see Fig. 15(b). With increasing stress triaxiality (45°, Fig. 15(c)) the damage appears more brittle.

6. Conclusion

The results presented in this publication with newly designed specimens made of thin sheets mark the reliable starting point of a comprehensive series of experiments which has to be extended over a wide range of stress states under consideration of the material orientation. Furthermore, these results can be used to quantify the damage behavior of plastic anisotropic metals. The consideration of the material orientation has to be taken into account when designing new geometries for specimens. The main findings and conclusions of this paper are:

- The anisotropy parameters of the Hill yield criterion are determined by a combined method based on tension and shear yield stresses as well as on the r-values. This leads to accurate prediction of the strain fields of the biaxial experiments.

Fig. 15. SEM images of fracture surface: (a) 0°, (b) 22.5° and (c) 45°.

- The newly presented specimens for thin sheets allow the systematic investigation of the material behavior of plastically anisotropic materials including damage and failure. The variation of the inclination of the holes offers a good possibility to include the material orientation in these investigations.
- The experiments presented here under 1/1 load are the promising starting point of an extensive series of tests in which the dependencies on the material orientation and on the load conditions must be analyzed.

Declaration of competing interest

The authors declare that they have no known competing financial interests or personal relationships that could have appeared to influence the work reported in this paper.

Data availability

Data will be made available on request.

References

Bai, Y., Wierzbicki, T., 2008. A new model of metal plasticity and fracture with pressure and lode dependence. Int. J. Plast. 24 (6), 1071–1096.

Barlat, F., Aretz, H., Yoon, J.W., Karabin, M.E., Brem, J.C., Dick, R.E., 2005. Linear transfomation-based anisotropic yield functions. Int. J. Plast. 21 (5), 1009–1039.

Brünig, M., Brenner, D., Gerke, S., 2015. Stress state dependence of ductile damage and fracture behavior: experiments and numerical simulations. Eng. Fract. Mech. 141, 152–169.

Brünig, M., Chyra, O., Albrecht, D., Driemeier, L., Alves, M., 2008. A ductile damage criterion at various stress triaxialities. Int. J. Plast. 24 (10), 1731–1755.

Brünig, M., Gerke, S., Hagenbrock, V., 2013. Micro-mechanical studies on the effect of the stress triaxiality and the lode parameter on ductile damage. Int. J. Plast. 50, 49–65.

Brünig, M., Gerke, S., Koirala, S., 2021. Biaxial experiments and numerical analysis on stress-state-dependent damage and failure behavior of the anisotropic aluminum alloy EN AW-2017A. Metals 11 (8), 1214.

Brünig, M., Gerke, S., Zistl, M., 2019. Experiments and numerical simulations with the H-specimen on damage and fracture of ductile metals under non-proportional loading paths. Eng. Fract. Mech. 217, 106531.

Brünig, M., Koirala, S., Gerke, S., 2022. Analysis of damage and failure in anisotropic ductile metals based on biaxial experiments with the H-specimen. Exp. Mech. 62, 183–197.

Brünig, M., Zistl, M., Gerke, S., 2020. Biaxial experiments on characterization of stress-state-dependent damage in ductile metals. Prod. Eng. 14 (1), 87–93.

Cauvin, L., Raghavan, B., Jin, J., Bouvier, S., Wang, X., Meraghni, F., Alves, J.L., 2022. Investigating the plastic anisotropy and hardening behavior of a commercial Zn–cu–ti alloy: Experimental & modeling approach. Mech. Mater.: Int. J. 164 (6), 104103.

Daehn, G., Cao, J., Kinsey, B., Tekkaya, E., Vivek, A., Yoshida, Y. (Eds.), 2021. Forming the Future. In: The Minerals, Metals & Materials Series, Springer International Publishing, Cham, http://dx.doi.org/10.1007/978-3-030-75381-8.

Driemeier, L., Brünig, M., Micheli, G., Alves, M., 2010. Experiments on stress-triaxiality dependence of material behavior of aluminum alloys. Mech. Mater. 42 (2), 207–217.

Dunand, M., Mohr, D., 2011. On the predictive capabilities of the shear modified gurson and the modified mohr–Coulomb fracture models over a wide range of stress triaxialities and lode angles. J. Mech. Phys. Solids 59 (7), 1374–1394.

Gao, X., Wang, T., Kim, J., 2005. On ductile fracture initiation toughness: effects of void volume fraction, void shape and void distribution. Int. J. Solids Struct. 42 (18–19), 5097–5117.

Gao, X., Zhang, G., Roe, C., 2010. A study on the effect of the stress state on ductile fracture. Int. J. Damage Mech. 19 (1), 75–94.

Gerke, S., Adulyasak, P., Brünig, M., 2017. New biaxially loaded specimens for the analysis of damage and fracture in sheet metals. Int. J. Solids Struct. 110-111, 209–218.

Gerke, S., Zistl, M., Bhardwaj, A., Brünig, M., 2019. Experiments with the X0-specimen on the effect of non-proportional loading paths on damage and fracture mechanisms in aluminum alloys. Int. J. Solids Struct. 163, 157–169.

Gerke, S., Zistl, M., Brünig, M., 2020. Experiments and numerical simulation of damage and fracture of the X0-specimen under non-proportional loading paths. Eng. Fract. Mech. 224, 106795.

Green, D.E., Neale, K.W., MacEwen, S.R., Makinde, A., Perrin, R., 2004. Experimental investigation of the biaxial behaviour of an aluminum sheet. Int. J. Plast. 20 (8–9), 1677–1706.
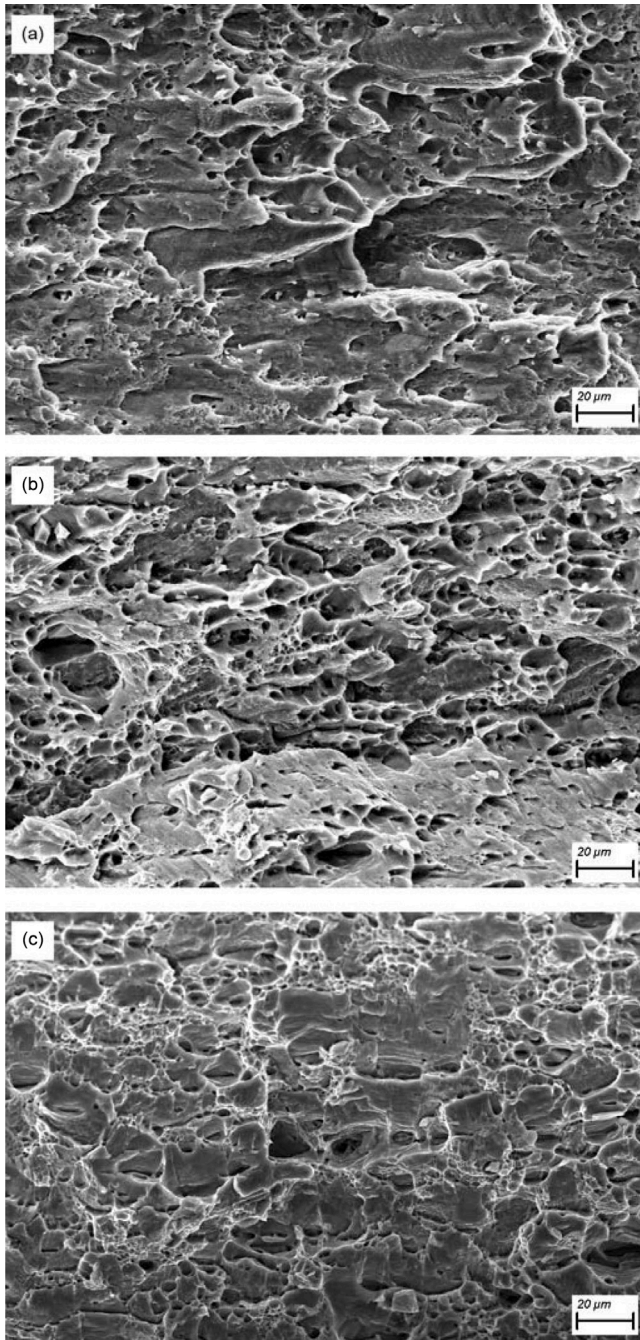
Ha, J., Baral, M., Korkolis, Y.P., 2018. Plastic anisotropy and ductile fracture of bake-hardened AA6013 aluminum sheet. Int. J. Solids Struct. 155, 123–139.

Hill, R., 1948. A theory of the yielding and plastic flow of anisotropic metals. Proc. R. Soc. Lond. A 193 (1033), 281–297.

Hu, Q., Yoon, J.W., Manopulo, N., Hora, P., 2021. A coupled yield criterion for anisotropic hardening with analytical description under associated flow rule: modeling and validation. Int. J. Plast. 136 (2), 102882.

Kong, X., Helfen, L., Hurst, M., Hänschke, D., Missoum-Benziane, D., Besson, J., Baumbach, T., Morgeneyer, T.F., 2022. 3D in situ study of damage during a 'shear to tension' load path change in an aluminium alloy. Acta Mater. 117842.

Kulawinski, D., Nagel, K., Henkel, S., Hübner, P., Fischer, H., Kuna, M., Biermann, H., 2011. Characterization of stress–strain behavior of a cast TRIP steel under different biaxial planar load ratios. Eng. Fract. Mech. 78 (8), 1684–1695.

Kuwabara, T., 2007. Advances in experiments on metal sheets and tubes in support of constitutive modeling and forming simulations. Int. J. Plast. 23 (3), 385–419.

Li, H., Fu, M.W., Lu, J., Yang, H., 2011. Ductile fracture: Experiments and computations. Int. J. Plast. 27 (2), 147–180.

Lin, S.B., Ding, J.L., 1995. Experimental study of the plastic yielding of rolled sheet metals with the cruciform plate specimen. Int. J. Plast. 11 (5), 583–604.

Liu, Y., Kang, L., Ge, H., 2019. Experimental and numerical study on ductile fracture of structural steels under different stress states. J. Construct. Steel Res. 158, 381–404.

Lou, Y., Chen, L., Clausmeyer, T., Tekkaya, A.E., Yoon, J.W., 2017. Modeling of ductile fracture from shear to balanced biaxial tension for sheet metals. Int. J. Solids Struct. 112, 169–184.

Mamros, E.M., Mayer, S.M., Banerjee, D.K., Iadicola, M.A., Kinsey, B.L., Ha, J., 2022. Plastic anisotropy evolution of SS316L and modeling for novel cruciform specimen. Int. J. Mech. Sci. 234, 107663.

Pierron, F., Grédiac, M., 2021. Towards material testing 2.0. A review of test design for identification of constitutive parameters from full–field measurements. Strain 57 (1), 556.

Roth, C.C., Mohr, D., 2016. Ductile fracture experiments with locally proportional loading histories. Int. J. Plast. 79, 328–354.

Stoughton, T.B., Yoon, J.W., 2009. Anisotropic hardening and non-associated flow in proportional loading of sheet metals. Int. J. Plast. 25 (9), 1777–1817.

Tsutamori, H., Amaishi, T., Chorman, R.R., Eder, M., Vitzthum, S., Volk, W., 2020. Evaluation of prediction accuracy for anisotropic yield functions using cruciform hole expansion test. J. Manuf. Mater. Process. 4 (2), 43.

Wang, Z., Guines, D., Chu, X., Leotoing, L., 2022. Characterization of forming limits at fracture from shear to plane strain with a dedicated cruciform specimen. Int. J. Mater. Form. 15 (1).